

**Atomic structure and melting of Ni and Fe<sub>36</sub>Ni up to 400 GPa**D. N. Polsin <sup>1,2,\*</sup>, D. A. Chin <sup>1</sup>, T. S. Duffy <sup>3</sup>, M. Ginnane,<sup>1,2</sup> X. Gong,<sup>1</sup> L. E. Hansen,<sup>4</sup> A. J. LaPierre,<sup>1,5</sup> M. C. Marshall,<sup>1</sup> G. W. Collins,<sup>1,2,6</sup> and J. R. Rygg<sup>1,2,6</sup><sup>1</sup>Laboratory for Laser Energetics, University of Rochester, Rochester, New York 14623-1299, USA<sup>2</sup>Department of Mechanical Engineering, University of Rochester, Rochester, New York 14627, USA<sup>3</sup>Department of Geosciences, Princeton University, Princeton, New Jersey 08544, USA<sup>4</sup>Sandia National Laboratories, PO Box 5800, Albuquerque, New Mexico 87185-1189, USA<sup>5</sup>Department of Chemistry, University of Rochester, Rochester, New York 14627, USA<sup>6</sup>Department of Physics and Astronomy, University of Rochester, Rochester, New York 14627, USA

(Received 14 February 2024; revised 24 April 2024; accepted 6 June 2024; published 27 June 2024)

Iron, nickel, and their alloys are critically important materials for industrial and technological applications due to their unique magnetic properties, strength, and thermal expansion. In this study, lasers were used to compress and heat Fe<sub>36</sub>Ni alloy (36 wt% Ni) and pure nickel up to the melting temperature using a combination of shock and ramp compression. The structure was measured using nanosecond *in situ* x-ray diffraction, and simultaneous velocimetry was used to measure the pressure up to 454 GPa. A mixed face-centered-cubic (fcc) solid–liquid phase in Fe<sub>36</sub>Ni at 311 GPa provides experimental evidence that, compared with pure iron, the incorporation of nickel expands the stability field of the fcc phase to the melting curve. At lower temperatures, a mixed fcc and hexagonal-close-packed (hcp) phase is observed in ramp-compressed Fe<sub>36</sub>Ni at 278 GPa. At the higher compressions, a structure inconsistent with fcc, hcp, and body-centered cubic is observed. In the case of pure Ni, the fcc phase is stable under ramp compression up to 402 GPa.

DOI: [10.1103/PhysRevB.109.214112](https://doi.org/10.1103/PhysRevB.109.214112)**I. INTRODUCTION**

Iron (Fe) and nickel (Ni) are 3*d* transition metals that have numerous technological applications when alloyed due to their manipulable strength, thermal-expansion coefficients, and gas and magnetic permeabilities [1,2]. These elements are also the primary components of Earth's core, where they experience extreme pressures and temperatures (136 to 364 GPa, 4000 to 6500 K) [3]. The core is mainly composed of Fe alloyed with 5%–15% Ni and some lighter elements including H, C, S, O, and Si [3,4]. While the average nickel content of iron meteorites is  $\approx 9.1$  wt%, there are some meteorites that contain higher nickel contents of 16 to 35 wt% [5].

Pure iron has been the focus of numerous high-pressure studies with measurements of the structure and equation of state (EOS) well beyond the conditions of Earth's crystalline inner core [6–13]. Iron is stable in the body-centered cubic (bcc,  $\alpha$ ) structure at ambient conditions and transforms to a hexagonal-close-packed (hcp,  $\epsilon$ ) phase upon compression to 13 GPa [14]. The  $\epsilon$  phase is stable over a wide range of pressures up to at least 300 GPa at room temperature [15] and up to 1 TPa along the melting curve [6].

Pure nickel has been predicted to remain in the face-centered-cubic (fcc) phase to terapascal conditions [16]. The fcc phase has been observed up to 368 GPa and room temperature under static compression [17]. Experiments have explored the high-pressure EOS [18], melting curve [19,20],

magnetic properties [21], and liquid structure [19] of Ni. Theoretical calculations have also explored the phase stability, thermodynamic, and elastic properties of Ni [22,23]. One study has proposed that, while the fcc phase remains stable at lower temperatures, a bcc phase of nickel could be stable above 140 GPa and 4000 K [22]. Although Ni is believed to be a canonical fcc element to very high pressures, there are predictions that Ni will transform into an insulator at 34 TPa [16] and that its robust van Hove singularity in its electronic band structure may be important in models of Earth's geomagnetism [24].

Studies of the effect of alloying on the structure in FeNi alloys show a sensitive dependence on Ni concentration [15,25–27]. At ambient conditions, Fe-Ni alloys with less than 25 at.% of Ni crystallize in the bcc phase, and the higher Ni content alloys crystallize in the fcc phase [1,15]. Fe-Ni alloy transforms to an hcp or hcp + fcc mixed phase upon compression (7 to 150 GPa depending on composition) [15]. At high pressures and upon heating to 2000 K (below the melting curve), various compositions (18.4, 24.9, 29.8, 35.7, and 50 wt% Ni) of Fe-Ni alloy transform to a mixture of hcp and fcc phases and eventually pure fcc with increasing temperature [15]. This is in contrast with pure Fe where the fcc phase is stable over a relatively small range of pressures upon heating from the ambient bcc phase. At higher temperatures approaching the melting curve (3400 K), measurements on Fe<sub>90</sub>Ni<sub>10</sub> find that it adopts a bcc structure at 225 GPa [25] and computational studies suggest bcc Fe could be stable due to diffusion mechanisms [28,29] or the distribution of Ni in the Fe matrix [30]. Shock-wave data on Fe-Ni alloys

\*Contact author: dpol@lle.rochester.edu

with 10, 18, and 26 wt% Ni exist up to 200 GPa [31]. Additionally, there have been studies of iron-nickel meteorites under shock compression [32–35] as well as an interest in the shock-induced microstructure of natural and recovered iron meteorite samples [36–38].

The studies presented here used an fcc alloy called Invar<sup>®</sup> (Fe<sub>36</sub>Ni) that is well known for its remarkably low thermal-expansion coefficient at ambient conditions. The Noble Prize in physics was awarded in 1920 for its discovery [39]. X-ray absorption measurements in laser-heated diamond anvil cells (DACs) find that Fe<sub>20</sub>Ni and Fe<sub>36</sub>Ni both melt in the fcc phase and their melting curves coincide up to 60 GPa, demonstrating that the higher Ni content does not significantly affect the melting curve of Fe-Ni alloy up to those conditions [26]. High-pressure dynamic compression experiments on Fe<sub>36</sub>Ni are limited to 16 GPa [40–42] and no tabular EOS models exist for the iron-nickel binary system.

In this study, x-ray diffraction (XRD) measurements on laser-compressed Fe<sub>36</sub>Ni and pure nickel performed across a large range of pressure and entropy states reveal that the fcc structure is stabilized through the addition of Ni as well as an increase in temperature. The observation of fcc solid and liquid coexistence provides experimental evidence that the fcc phase is stable up to the melting curve. This is in contrast with pure Fe that melts in the hcp phase [6,10]. At lower temperatures, a mixed fcc and hcp phase is observed at 278 GPa and an unknown phase is observed at 367 GPa. Pure Ni is fcc up to 402 GPa.

## II. METHODS

To compress Fe<sub>36</sub>Ni and nickel to the very high pressures and temperatures relevant to Earth's inner core (330 GPa, ≈5000 K) and beyond, we simultaneously compress and heat the alloy samples using a combination of laser-driven shock and ramp compression. This section of the paper is divided into two sections corresponding to ramp-compression and shock-release-ramp compression experiments. The first were designed to nearly isentropically compress the samples, enabling higher compressions and lower temperatures than shock compression [Figs. 1(a)–1(d)]. The second set of experiments used a combination of shock and ramp compression to heat the samples up to the melting curve [Figs. 1(e)–1(h)].

### A. Ramp-compression experiments

Experiments were performed on the Omega EP laser at University of Rochester's Laboratory for Laser Energetics [43]. Laser energies up to 1.1 kJ were delivered using temporally shaped 351-nm laser pulses. A single beam irradiated the targets over 10 ns [Fig. 1(b)]. It was smoothed using distributed phase plates producing an 1100-μm-diameter focal spot with a super-Gaussian intensity distribution. The laser power was continuously increased to peak intensities of up to  $1.2 \times 10^{13}$  W/cm<sup>2</sup>. An additional beam with a nominally steady 1.25-ns pulse irradiated a separate 2-mm × 2-mm pure-Fe foil backlighter target to produce 6.685-keV (1.855 Å) heliumlike (He<sub>α</sub>) x rays that probed the compressed sample [44].

To measure the structure of compressed Fe<sub>36</sub>Ni and Ni, x-ray diffraction (XRD) data were collected using the powder XRD image plate (PXRDIP) diagnostic that is described in detail in Refs. [45,46]. The target is held on the front face of a stainless-steel box that is lined with image plates [47]. Pure Fe (12.5-μm) and Kapton (25-μm) filters are inserted in front of the image plate detectors to protect them from debris, attenuate high-energy background photons just above the Fe *K*-edge and low-energy background photons (approximately <3 keV). The target is mounted on a 100-μm-thick tungsten or platinum plate with a 300-μm-diameter pinhole aperture to provide x-ray collimation and to restrict the field of view of the image plates to the center of the 1100-μm driven region of the target. The x-ray source is positioned at 22.3° with respect to the target normal as shown in Fig. 1(a). Diffraction peaks from the edges of the pinhole aperture provide an *in situ* calibration of the  $2\theta$  scattering angle. The ambient bcc W and fcc Pt reference XRD patterns are chosen to minimize overlap with the high-pressure XRD from the sample. The interatomic lattice plane spacings are calculated using the Bragg condition. The reported error in the  $2\theta$  scattering angle is calculated using the difference between the expected  $2\theta$  and calculated  $2\theta$  of the calibration pinhole diffraction lines using the best-fit geometrical parameters. An additional error due to the uncertainty of the sample offset distance from the pinhole of ±10 μm is included. The  $2\theta$  standard deviation ranged from 0.1° to 0.2°.

The targets were designed so that the wave interactions between the various layers nearly isentropically compressed the samples while optimizing the XRD signal. The samples were 15.0-μm-thick Fe<sub>36</sub>Ni alloy and pure-Ni (8.9-g/cm<sup>3</sup>) foils obtained from Goodfellow. This thickness is approximately one optical depth at 6.685 keV and maximizes the XRD signal for the transmission pinhole camera XRD configuration used here. An ambient XRD pattern collected with a Philips X'Pert High Resolution Materials Research Diffractometer confirmed the initial fcc phase of Fe<sub>36</sub>Ni with a lattice parameter,  $a = 3.58 \pm 0.01$  Å, corresponding to a density of 8.2 g/cm<sup>3</sup>. The sample foil was sandwiched between a 35-μm-thick ⟨110⟩-oriented single-crystal diamond ablator and a 100-μm-thick ⟨100⟩-oriented single-crystal LiF window [Fig. 1(a)]. The single crystals are chosen to preclude producing extended diffraction lines for the non-Fe<sub>36</sub>Ni and Ni layers.

The pressure in the sample is calculated using measurements of the sample-LiF interface velocity. A line-imaging velocity interferometer for any reflector (VISAR) [48] detects the Doppler shifts of a 532-nm probe beam reflected off the sample-LiF interface as a function of time. The signal passes through a pair of interferometers, and one of the resulting interferograms is shown in Fig. 1(c). The ramp-compression wave breaks out of the sample at ≈5 ns and then smoothly accelerates the sample-LiF interface up to nearly 7 km/s when it is probed with XRD. The sensitivities of the two VISAR channels are 5.4205 and 2.1773 μm ns<sup>-1</sup> fringe<sup>-1</sup>. The apparent sample-LiF interface velocity is corrected to give the true velocity using the LiF refractive index data from Ref. [49].

The extracted velocities are shown in Fig. 1(d) and are used as a boundary condition in a method-of-characteristics calculation [50] to infer the pressure in the sample during

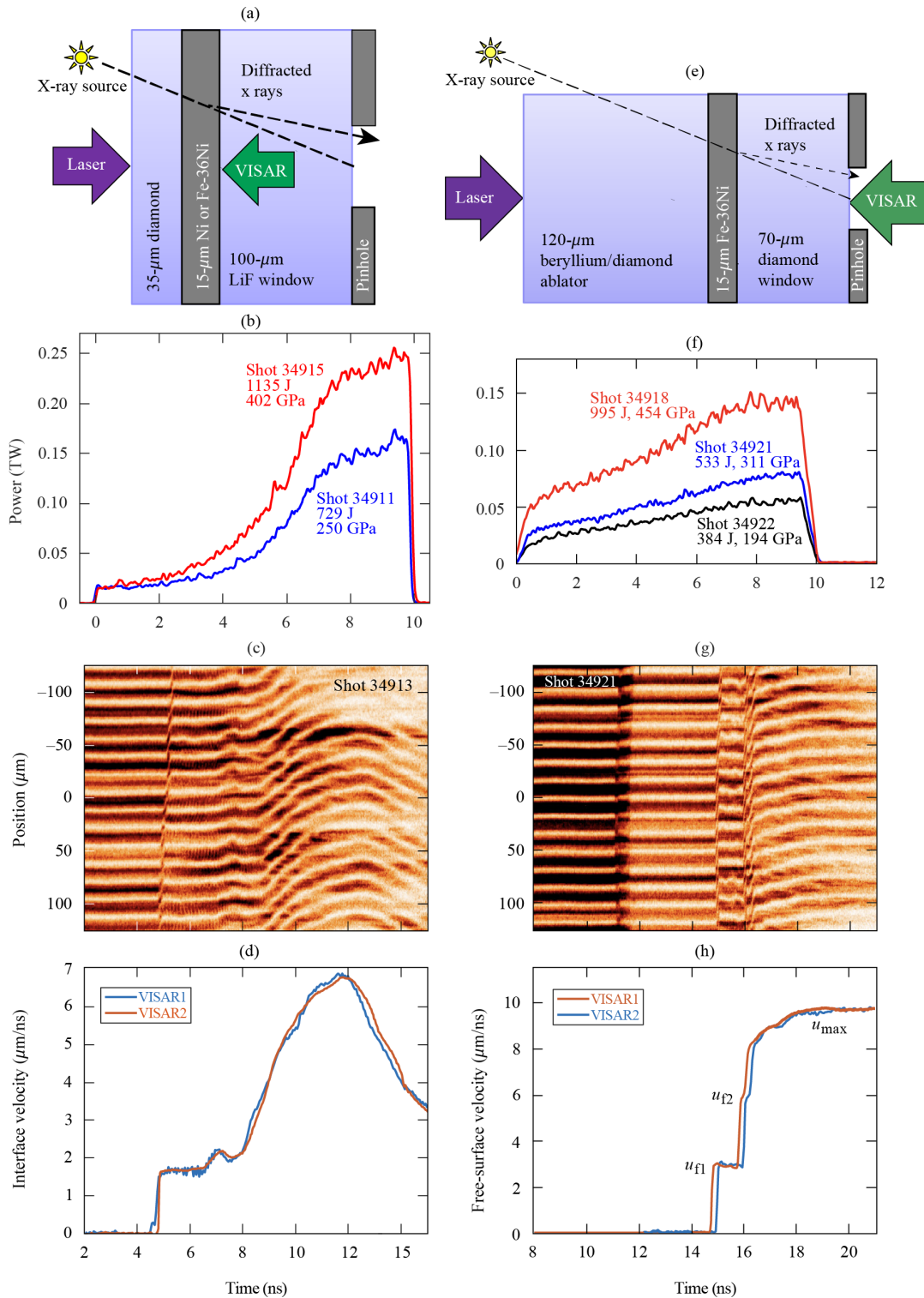


FIG. 1. (a) Schematic of the ramp-compression XRD targets. The diamond transmits the ramping pressure wave into the sample, which is tamped by the LiF window. The LiF window is transparent to the VISAR (velocity interferometer system for any reflector) probe beam throughout the experiment. The x rays are incident at a nominal angle of 22.3 degrees and are flashed at peak pressure. (b) Representative laser pulse shapes used to ramp-compress Fe<sub>36</sub>Ni and pure Ni. (c) Streaked line-imaging VISAR interferogram, where the fringe shifts correspond to the velocity of the sample-LiF interface. (d) The interface velocities extracted from the two VISAR channels. A weak initial shock arrives at the interface around 5 ns and the wave interactions between the diamond and LiF substrates nearly isentropically increase the velocity and pressure to 278 GPa. (e) Schematic of the shock-release-ramp Fe<sub>36</sub>Ni XRD targets. (f) The laser pulse shapes used to compress and heat Fe<sub>36</sub>Ni. The rapid increase in the laser power launches a stronger initial shock wave into the target compared with those shown in panel (b). (g) Streaked line-imaging VISAR interferogram, where the fringe shifts after 12 ns correspond to the diamond window free-surface velocity. (h) The free-surface velocities extracted from the two VISAR channels (only shown after 12 ns).

the x-ray probe time. The LiF SESAME 7271v3 principal isentrope [51] and the pure-Fe LEOS 260 principal isentrope were used as the EOS models for the window and the sample. Because the sample was thin and compressed over a relatively long timescale, the pressure of the FeNi sample is independent from its EOS but does rely on the window EOS. The reported errors in the mean pressure are the quadrature sum of the random error due to the standard deviation of pressures inferred from each VISAR leg, a systematic 3% error in the pressure–density EOS of LiF [49], a systematic 0.3% error in the refractive index of LiF, and the random uncertainty due to the mean of the ensemble of pressures within the finite thickness of the sample over the duration of the x-ray probe. The total reported uncertainty ranged from 6.5% to 10.1%.

### B. Shock-release-ramp experiments

To probe the structure of Fe<sub>36</sub>Ni up to its melting point, modifications to the target design and laser power allowed for a shock-release-ramp compression path. Three representative laser pulse shapes are shown in Fig. 1(f). The initial rapid increase in laser power launches a shock wave into the target that compresses and heats the Fe<sub>36</sub>Ni to a state on the principal Hugoniot. The first shock pressures ranged from 183 to 428 GPa. The laser power is then increased linearly to peak intensities of up to  $1.1 \times 10^{13}$  W/cm<sup>2</sup> that sustains the pressure at the ablation front as the sample compresses to its final pressure state.

The targets were designed so that the applied laser power allowed for the Fe<sub>36</sub>Ni to be compressed to increasing pressure–temperature conditions up to the melting curve. The Fe<sub>36</sub>Ni foil was sandwiched between a 120- $\mu$ m-thick beryllium or (110)-oriented single-crystal diamond ablator and a 70- $\mu$ m-thick (110)-oriented single-crystal diamond window [Fig. 1(e)]. The sample follows a shock-release-ramp thermodynamic path. The Fe<sub>36</sub>Ni is first compressed and heated to a state on the Hugoniot. It then releases as the shock enters the diamond window—ignoring the interaction with the thin epoxy layer. A reverberation sequence between the shocked Be (or diamond) ablator and diamond window then nearly isentropically compresses the Fe<sub>36</sub>Ni to its final pressure state when it is probed with XRD. The temperature is not measured in these experiments but it is assumed that the initial shock sets the entropy of the system.

The pressure is calculated in two distinct ways to bound the conditions in sample. Similar to the ramp-compression experiments, both methods use measurements of the target velocity. Because the diamond window becomes opaque to the VISAR probe beam for stresses above the Hugoniot elastic limit, the VISAR measures the diamond free surface (diamond–vacuum interface) velocity as shown in Figs. 1(g) and 1(h). The initial shock breaks out of the sample at 11.5 ns, rendering the diamond opaque. The fringe motion, now corresponding to the diamond free surface, is stationary until 15 ns when the free surface is then accelerated in a multishock sequence up to  $\approx 10$   $\mu$ m/ns. The first method uses the measured elastic wave free-surface velocity  $u_{f1}$ , plastic wave free-surface velocity  $u_{f2}$ , the maximum free-surface velocity  $u_{max}$ , the diamond window thickness, and the breakout times into and out of the diamond to calculate the pressure behind the plastic wave in

the diamond assuming a steady shock wave [52]. The particle velocity to free-surface velocity relation  $u_f = 2u_p$  is assumed and the Rankine–Hugoniot equations are applied twice for the two-shock system. The Fe<sub>36</sub>Ni is then assumed to be ramp compressed from this shock-release state to  $u_{max}$  using an experimental ramp-compression EOS of diamond [53].

The second method is used to calculate the pressure distribution within the Fe<sub>36</sub>Ni sample using the same free-surface velocity but in a method-of-characteristics algorithm [50], which assumes that each shock originates at the diamond free surface. The inputs of the calculation include measurements of the diamond and Fe<sub>36</sub>Ni thicknesses and the experimental ramp EOS of diamond [53]. The results from these two methods are consistent within 8% in pressure due to the similar compressibilities of the diamond shock wave and ramp data [53]. The uncertainties reported in the pressure include an 8% error due to assumptions in the thermodynamic path,  $\pm 5$ - $\mu$ m error in the diamond thickness, and the standard deviation in the pressures inferred from each VISAR leg. The total standard error in the mean pressure is  $\approx 10\%$ . An additional +50-GPa systematic error due to diamond strength is included [4]. This is related to the assumption that  $u_f = 2u_p$ , which has been observed to be  $u_f = 1.56u_p$  for (110) diamond below 300 GPa [52].

## III. RESULTS

### A. Ramp-compression experiments

The XRD data for ramp-compressed nickel shows that it remains in the fcc phase to 402 GPa (Fig. 2). Two XRD peaks from the compressed Ni are observed and indexed as the fcc (111) and (200) reflections. The same two peaks are observed in a lower-pressure shot at 250 GPa. The  $d$  spacings as a function of pressure for the two experiments are shown in Fig. 3(a) and compared with those from the fcc, hcp, and bcc phases calculated from the Ni SESAME 3101 principal isentrope and Hugoniot. The data show excellent agreement with the fcc structure. Assuming the fcc phase, the densities are calculated for each XRD reflection and plotted in Fig. 3(b). As expected, the densities lie between the principal isentrope and Hugoniot consistent with ramp-compression with a weak initial shock. A summary of the pure Ni data is shown in Table I.

The XRD data on ramp-compressed Fe<sub>36</sub>Ni have additional reflections compared with the pure-Ni case. The image plate data at 278 and 367 GPa are shown in Fig. 4. Four reflections are observed between 60° and 75° at 278 GPa. The calculated  $d$  spacings are shown in Fig. 5 compared with the range of  $d$  spacings bounded by the Fe LEOS 260 principal isentrope and the Ni SESAME 3101 principal isentrope for the fcc, hcp, and bcc phases; an EOS table for Fe<sub>36</sub>Ni does not exist. At 278 GPa, the reflections can be indexed as a coexistence of fcc and hcp phases. The two weak hcp peaks cannot be explained by diffraction from an fcc structure but at a different wavelength. The x-ray source used in these experiments is inherently broadband with the weaker satellite peaks (e.g., Ly $_{\alpha}$ , 6.973 keV, 1.778 Å) capable of reaching  $\approx 10\%$  the intensity of the central He $_{\alpha}$  wavelength (6.6850 keV, 1.855 Å) [44]. Here we test whether diffraction from these higher-energy x rays could potentially explain the two

TABLE I. Pure Ni summary. The target dimension notation is material [thickness] and C is  $\langle 110 \rangle$ -oriented single-crystal diamond.

Shot	Pressure (GPa)	Target dimensions ( $\mu\text{m}$ )	$2\theta$ ( $^\circ$ )	Lattice parameter ( $\text{\AA}$ )	Density ( $\text{g/cm}^3$ )
34911	$250 \pm 25$	C[35]Ni[15]LiF[100]	$63.3 \pm 0.1$ $74.9 \pm 0.1$	$3.056 \pm 0.003$	$13.65 \pm 0.04$
34915	$402 \pm 38$	C[35]Ni[15]LiF[100]	$65.9 \pm 0.2$ $77.6 \pm 0.2$	$2.956 \pm 0.006$	$15.10 \pm 0.10$

lower-angle  $2\theta$  and lower-intensity diffraction peaks. The time-integrated x-ray source spectra for this particular experiment was measured and the intensity of the  $\text{Ly}_\alpha$  emission relative to the  $\text{He}_\alpha$  is  $\approx 2.5\%$ . The fcc (111) and fcc (200) peaks from the  $\text{He}_\alpha$  at  $2\theta = 64.2 \pm 0.2^\circ$  and  $74.9 \pm 0.2^\circ$  would appear at  $2\theta = 61.3^\circ$  and  $71.3^\circ$  at the  $\text{Ly}_\alpha$  wavelength. These values are not in agreement with our measured  $2\theta$  of  $60.3 \pm 0.2^\circ$  and  $69.2 \pm 0.2^\circ$ , respectively. Furthermore, the texture of the weaker peaks are not identical to the more intense peaks. Given these observations, the reflections at 278 GPa are assigned to the hcp (010), fcc(111), hcp (011), and fcc (200).

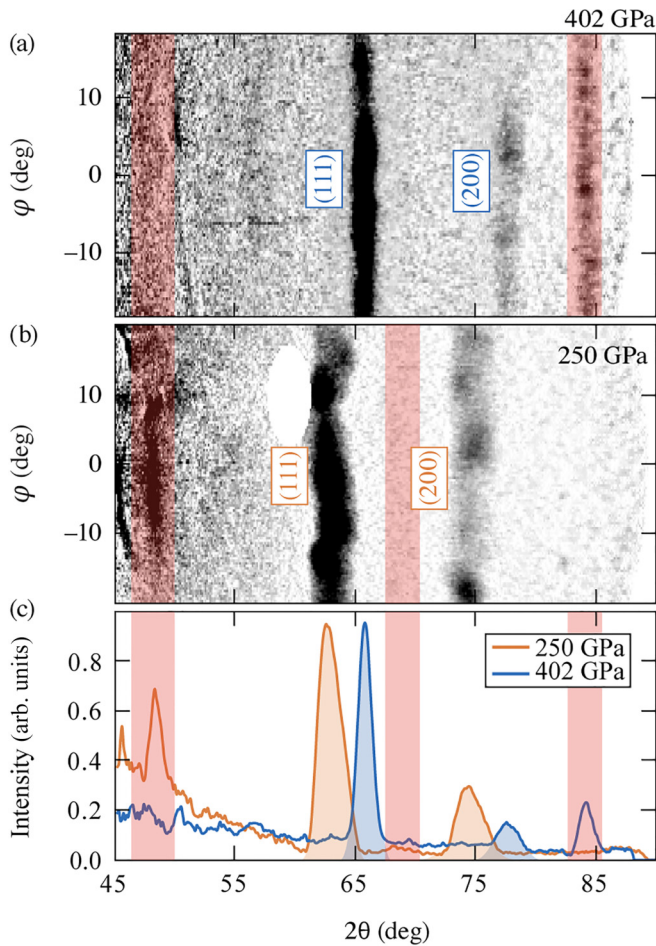


FIG. 2. Background subtracted  $2\theta$ - $\phi$  projections of XRD patterns for ramp-compressed fcc Ni at (a) 402 GPa and (b) 250 GPa. The red bands mask XRD lines from the ambient density pinhole calibrants. (c) The integrated XRD patterns showing the clear shift of the fcc (111) and (200) peaks to higher  $2\theta$  with increasing pressure.

The coexistence of the hcp and fcc phases at 278 GPa is consistent with static-compression experiments that observed this coexistence with compression in the same alloy at 102 to 291 GPa and 300 K [15]. In the static work, the hcp peaks disappear when the fcc + hcp mixture was heated and the estimated transition temperature to pure fcc is  $\approx 1200$  K. In these experiments, the initial shock observed at the

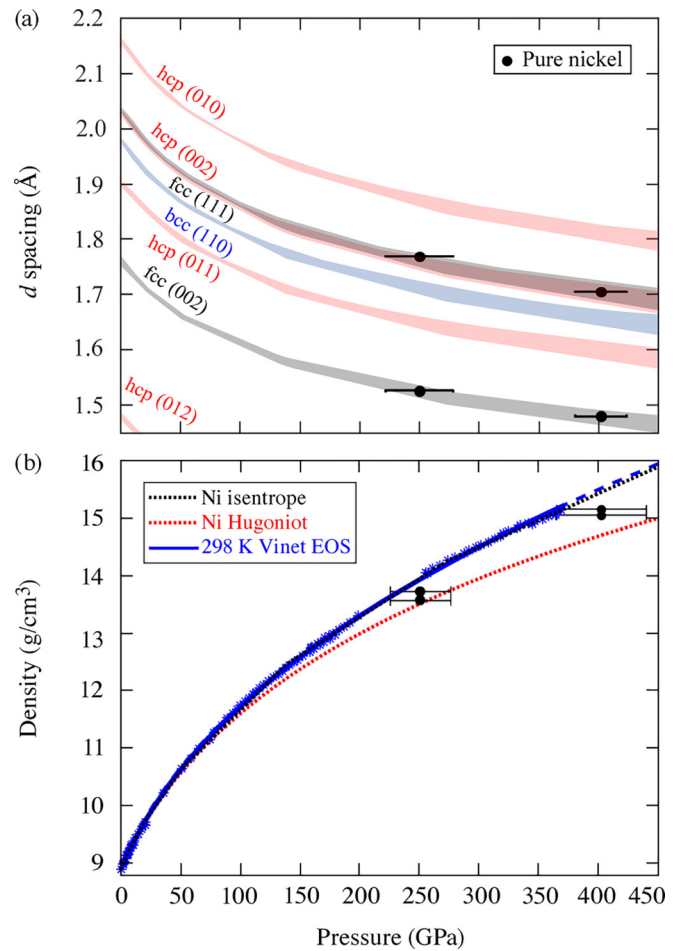


FIG. 3. (a) A comparison of the measured  $d$  spacing versus pressure from this work (solid circles) and those bounded by the nickel principal isentrope and Hugoniot from SESAME 3101 (continuous bands) for the fcc (black), hcp (red), and bcc (blue) phases. The hcp (002) and fcc (111) phases have identical  $d$  spacing so they are plotted slightly offset for clarity. (b) The Ni density compared with the SESAME 3101 principal Hugoniot (red) and isentrope (black) and the Vinet EOS fit to static-compression room-temperature pressure-volume data (blue stars) to 368 GPa (blue solid, dash extrapolation) [18].

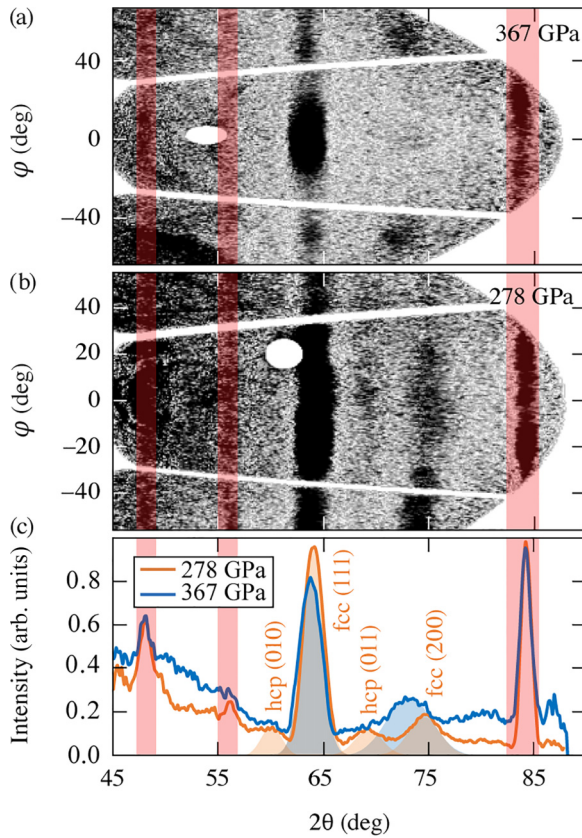


FIG. 4. Background-subtracted  $2\theta$ - $\phi$  projections of XRD patterns for ramp-compressed  $\text{Fe}_{36}\text{Ni}$  at (a) 367 GPa and (b) 278 GPa. The red bands mask XRD lines from the ambient density Pt calibrant. (c) The integrated XRD patterns show four peaks at 278 GPa that are indexed as a mixture of fcc and hcp phases (orange). At 367 GPa, two peaks are observed (blue). The lowest angle does not shift to a higher  $2\theta$  with compression and the higher angle peak shifts to a lower  $2\theta$  indicating that a phase transformation has occurred.

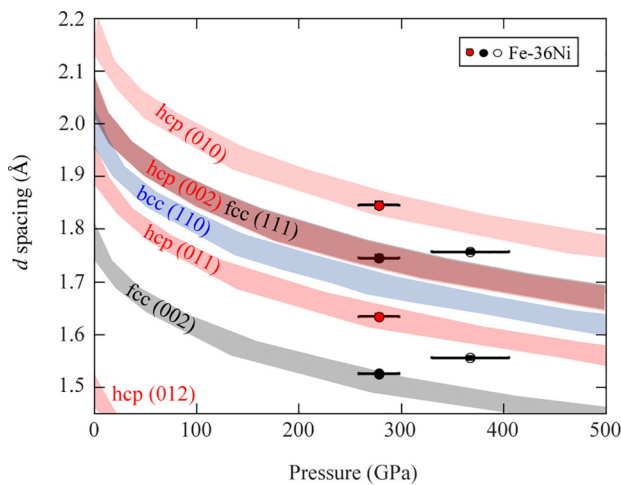


FIG. 5. A comparison of the measured  $d$  spacing versus pressure from this work (solid circles) and the  $d$  spacings bounded by the nickel principal isentrope from SESAME 3101 and the Fe LEOS 260 principal isentrope (bands) for the fcc (black), hcp (red), and bcc (blue) phases. The color of the data points represents the assigned structure (black: fcc, red: hcp, unfilled: unknown).

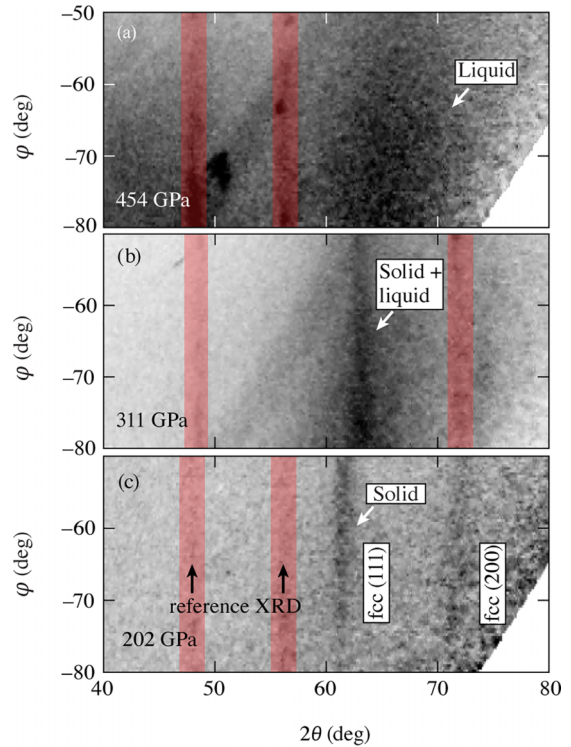


FIG. 6. X-ray diffraction image-plate data for  $\text{Fe}_{36}\text{Ni}$  at (a) 454 GPa (shot 34918), (b) 311 GPa (shot 34921), and (c) 202 GPa (shot 36021) showing x-ray diffraction from the liquid, solid-liquid-coexistence, and solid phases. The red shaded regions mask the reference XRD lines.

$\text{Fe}_{36}\text{Ni}$ -LiF interface [Fig. 1(d), particle velocity  $u_p = 1.6$  km/s] corresponds to an initial shock pressure and temperature of  $\approx 60$  GPa and  $\approx 1000$  K, suggesting a similar lower-bound transition temperature.

At higher pressure, only two diffraction peaks are observed. As seen in Fig. 5, the  $d$  spacings of the two peaks do not show agreement with the  $d$  spacings of the fcc, hcp, and bcc phases. A comparison of the XRD pattern to those from the fcc, hcp, dhcp, bcc, and a strained fcc phase are shown in the Supplemental Material [54] (including Refs. [6,15,26,55,56]). None of them provide an adequate match to the data. The data at this pressure have decreased signal-to-background compared with the lower-pressure data at least in part because the image plates had stainless-steel filtering rather than pure Fe filtering and hence a different spectrum of background x rays were transmitted. But the filter material would have no effect on the  $2\theta$  position of the peaks. Indexing these two peaks as the fcc (111) and (200) reflections yields unreasonably small and different densities at these conditions, ruling out the fcc phase. In addition, a marked change in the texture is observed compared with the lower-pressure data and high-pressure phase transformations are often accompanied with a change in texture [57–60]. Therefore, we conclude that a phase transformation is occurring in ramp-compressed  $\text{Fe}_{36}\text{Ni}$  between 278 and 367 GPa. A summary of the ramp-compressed  $\text{Fe}_{36}\text{Ni}$  data is shown in Table II.

TABLE II. Ramp-compressed  $\text{Fe}_{36}\text{Ni}$  summary. The target dimension notation is material [thickness] and C is  $\langle 110 \rangle$ -oriented single-crystal diamond. The lattice parameters and density of the high-pressure phase are unknown.

Shot	Pressure (GPa)	Target dimensions ( $\mu\text{m}$ )	$2\theta$ ( $^\circ$ )	Lattice parameter ( $\text{\AA}$ )	Density ( $\text{g/cm}^3$ )
34913	$278 \pm 18$	C[35] $\text{Fe}_{36}\text{Ni}$ [15]LiF[100]	$60.3 \pm 0.2$	$3.036 \pm 0.008$ (fcc)	$13.5 \pm 0.2$ (fcc)
			$64.2 \pm 0.2$	$a = 2.130 \pm 0.007$ (hcp)	$13.6 \pm 0.1$ (hcp)
			$69.2 \pm 0.2$	$c/a = 1.65 \pm 0.03$ (hcp)	
			$74.9 \pm 0.2$		
34914	$367 \pm 36$	C[35] $\text{Fe}_{36}\text{Ni}$ [15]LiF[100]	$63.8 \pm 0.2$ $73.2 \pm 0.2$		

### B. Shock-release-ramp experiments

Examples of the shock-ramp XRD data in the liquid, the coexistence of fcc and liquid, and the solid fcc phases for  $\text{Fe}_{36}\text{Ni}$  are shown in Figs. 6(a)–6(c), respectively. The XRD data are warped into a  $2\theta$ – $\phi$  space, where  $\phi$  is the azimuthal angle around the Debye–Scherrer ring. The data shown are the raw images; no background subtraction has been applied in order to show the extended character of the liquid scattering. Figure 6(c) shows the XRD data at 202 GPa where the lines can be indexed as the fcc (111) and (200) reflections. As the temperature and pressure are increased to 311 GPa [Fig. 6(b)], a diffuse feature coincident with the (111) reflection emerges. We interpret this datum as a mixture of the liquid and solid

phases [6,62]. At the highest pressures and temperatures, the solid Bragg peaks disappear completely (except the reference XRD lines) and only the diffuse liquid scattering is observed.

We find that the solid XRD data are best fit to the fcc structure. The  $\text{Fe}_{36}\text{Ni}$  pressure inferred from VISAR versus the density deduced from the XRD data are shown in Fig. 7. The densities assuming the single solid Bragg peak is indexed as the fcc (111) give reasonable densities compared with the theoretical EOS models for iron and nickel. To rule out a high-temperature, high-pressure hcp or bcc phase, the peak is indexed as the hcp (011) or bcc (110) reflections, but the densities are unreasonably small at these conditions. Because the  $d$  spacing of the hcp (002) and fcc(111) are identical, we cannot rule out that the single peak is from a highly textured hcp phase but the hcp (011) peak is expected to be more intense for an ideal powder. The shock-release-ramp data are summarized in Table III.

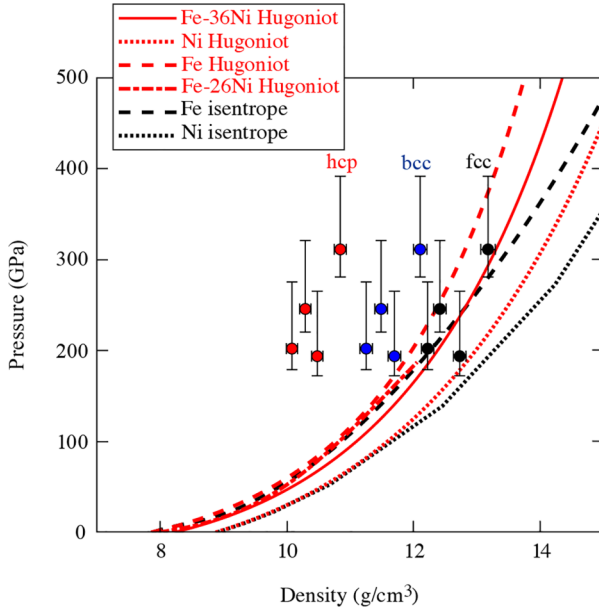


FIG. 7. A comparison of the measured pressure versus density from this work (solid circles) to the Ni principal isentrope (dotted black curve) and Hugoniot (dotted red curve) from SESAME 3101, the Fe LEOS 260 principal isentrope (dashed black curve) and Hugoniot (dashed red curve), the fit to shock wave data for Fe-26Ni to 187 GPa (dashed–dotted red curve) [31], and the  $\text{Fe}_{36}\text{Ni}$  Hugoniot calculated from a kinetic energy averaging model (red) [61]. The densities are calculated by indexing the lowest-angle Bragg reflection as the fcc (111) (black), hcp (011) (red), and bcc (110) (blue). The conclusion of this figure is that the XRD data are inconsistent with the expected pressure–density for the hcp and bcc structures, but are consistent with the fcc structure.

### IV. DISCUSSION

Fe-Ni alloys are expected to be an important component of the cores of the many terrestrial-type exoplanets that have been detected in recent years [63]. Although the average nickel content of iron meteorites is  $\approx 9.1$  wt%, there are some meteorites that contain higher nickel contents approaching that of Invar [5] such as the Santa Catharina meteorite (35 wt% Ni) [64,65]. High-nickel contents are thought to arise from core formation on highly oxidized parent bodies [66,67]. Since iron is more readily oxidized than nickel, oxidizing conditions can result in more Fe being incorporated into the mantle in the form of FeO and the resulting core is both smaller and enriched in nickel.

It has been suggested that rocky exoplanets may form under a wide range of possible oxidation states including highly oxidized conditions [68], which would be expected to produce a range of core compositions including potentially Ni-enriched cores as sometimes found in meteorites. Our work provides constraints on the atomic-level structure and melting for cores with such nickel-rich compositions. In addition, this work shows the feasibility of studying crystal structures and melting of compositions across the Fe-Ni system at the extreme pressures of Earth and exoplanetary cores, and this can be extended to the more Fe-rich compositions in future work.

These data and other high-pressure iron-nickel structural data are compiled in a temperature-composition phase diagram at  $275 \pm 57$  GPa [10,12,13,15,25] (Fig. 8). The melting curve from Kuwayama *et al.* [15] is scaled up to the re-

TABLE III. Shock-release-ramp-compressed Fe<sub>36</sub>Ni summary. The target dimension notation is material [thickness] and C is (110)-oriented single-crystal diamond. The reported pressure errors do not include the systematic error due to the diamond strength.

Shot	Pressure (GPa)	Target dimensions ( $\mu\text{m}$ )	$2\theta$ ( $^\circ$ )	Lattice parameter ( $\text{\AA}$ )	Density (g/cc)
34922	$194 \pm 21$	Be[120]Fe <sub>36</sub> Ni[15]C[70]	$62.5 \pm 0.2$ $73.6 \pm 0.2$	$3.096 \pm 0.008$	$12.7 \pm 0.1$
36021	$202 \pm 23$	C[120]Fe <sub>36</sub> Ni[15]C[70]	$61.6 \pm 0.2$ $72.4 \pm 0.2$	$3.138 \pm 0.008$	$12.2 \pm 0.1$
36015	$246 \pm 25$	C[120]Fe <sub>36</sub> Ni[15]C[70]	$62.1 \pm 0.2$ $72.7 \pm 0.2$	$3.122 \pm 0.008$	$12.4 \pm 0.1$
34921	$311 \pm 30$	Be[120]Fe <sub>36</sub> Ni[15]C[70]	$63.3 \pm 0.2$	$3.060 \pm 0.009$	$13.2 \pm 0.1$
34918	$454 \pm 47$	Be[120]Fe <sub>36</sub> Ni[15]C[70]	Melted		

ported melting temperature from pure-Fe shock experiments observed at 242 GPa and 5560 K [10]. At low temperatures near 1000 K, we observe the hcp + fcc phase in agreement with static-compression data. With increasing shock strength, the hcp phase disappears and only fcc is observed. At higher temperatures, our measurement of the fcc phase along the melting curve at 311 GPa provides an upper bound on the fcc–hcp–liquid triple point. The location of this triple point has important implications for the structure of the cores of Earth and rocky exoplanets and suggests that a Ni-enriched core with 36 wt% Ni would crystallize in the fcc phase.

## V. CONCLUSION

In this work, we observe that the incorporation of nickel in the Fe-Ni system and elevated temperatures stabilizes

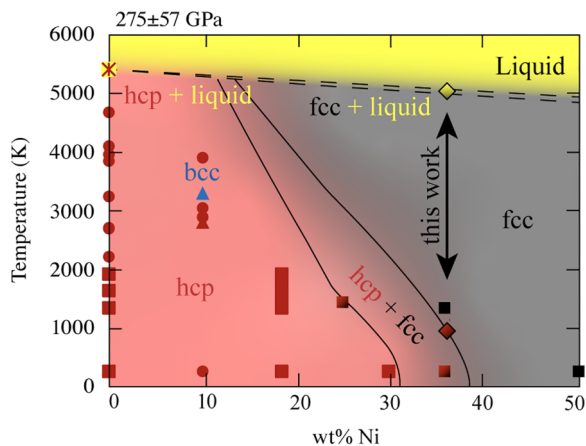


FIG. 8. Temperature-composition phase diagram of the iron-nickel alloy system at  $275 \pm 57$  GPa. The data are color coded according to their phase (fcc: black, hcp: red, bcc: blue, liquid: yellow). A mixture of colors is used to designate coexistence. Data from this work are shown by the diamond markers. A mix of fcc and hcp phases is observed at  $\approx 1000$  K (red-black diamond) and the fcc-liquid phase on the melting curve (yellow-black diamond). Shock melting of pure iron in the hcp phase along the Hugoniot is shown by the cross from Turneure *et al.* [10]. Laser heated DAC data are shown from Kuwayama *et al.* [15] (squares), Dubrovinsky *et al.* [25] (triangles), and Tateno *et al.* [12,13] (circles). The melting curve from Ref. [15] is scaled up to the melting temperature from the pure Fe shock melting experiment by Ref. [10] and the fcc-liquid datum from this work is plotted along that curve.

the fcc structure over the competitive hcp and bcc structures. At low temperatures, the fcc and hcp phases coexist in ramp-compressed Fe<sub>36</sub>Ni at 278 GPa—consistent with static compression work [15]—but a textured phase inconsistent with the fcc, hcp, and bcc phases is observed at 367 GPa. Future work should investigate the role of significant compressions on Ni-rich Fe-Ni alloys where we find this new phase. In pure Ni, the fcc structure is stable up to 402 GPa, again confirming that Ni is an fcc stabilizer. Materials that do not undergo structural phase transitions under dynamic compression are often useful as standards in such experiments, but most materials do not retain their ambient structure up to multihundred GPa pressures. The persistence of the fcc structure in Ni up to 400 GPa under ramp compression makes it a candidate material as a dynamic-compression standard to extreme conditions. For shock-release-ramp experiments at higher temperatures, Fe<sub>36</sub>Ni transforms to pure fcc and remains stable up to the melting curve.

Our measurements reveal that alloying has a profound effect on phase stability across a large range of pressure and entropy states and demonstrates that the atomic-level structure and melting of Ni and Fe-Ni alloys can be extended to conditions at and above those achievable with conventional static-compression techniques. This capability provides new experimental constraints for testing and evaluating theoretical predictions of the crystal structure, equation of state, and melting of transition elements and their alloys at extreme conditions.

## ACKNOWLEDGMENTS

The authors thank the OMEGA EP team for laser operation, diagnostic support, and target development. The VISAR and PXRDIIP data were analyzed using LLNL’s Analyze-VISAR and AnalyzePXRDIIP codes. This material is based upon work supported by the Department of Energy [National Nuclear Security Administration] University of Rochester National Inertial Confinement Program under Award No. DE-NA0004144. This material is based upon work supported by the Center for Matter at Atomic Pressures (CMAP), a National Science Foundation (NSF) Physics Frontiers Center, under Award No. PHY-2020249.

This publication was prepared as an account of work conducted by the Laboratory for Laser Energetics and their sponsors. Neither the sponsors nor any agency thereof, nor

any of their employees, makes any warranty, express or implied, or assumes any legal liability or responsibility for the accuracy, completeness, or usefulness of any information, apparatus, product, or process disclosed, or represents that its use would not infringe privately owned rights. Reference herein to any specific commercial product, process, or service

by trade name, trademark, manufacturer, or otherwise does not necessarily constitute or imply its endorsement, recommendation, or favoring by the sponsors or any agency thereof. The views and opinions of authors expressed herein do not necessarily state or reflect those of the sponsors or any agency thereof.

- 
- [1] H. M. Ledbetter and R. P. Reed, *J. Phys. Chem. Ref. Data* **2**, 531 (1973).
- [2] A. Sahoo and V. R. R. Medicherla, *Mater. Today: Proc.* **43**, 2242 (2021).
- [3] T. S. Duffy, *Nature (London)* **479**, 480 (2011).
- [4] J. K. Wicks, R. F. Smith, D. E. Fratanduono, F. Coppari, R. G. Kraus, M. G. Newman, J. R. Rygg, J. H. Eggert, and T. S. Duffy, *Sci. Adv.* **4**, eaa05864 (2018).
- [5] J. Petrovic, *J. Mater. Sci.* **36**, 1579 (2001).
- [6] R. G. Kraus, R. J. Hemley, S. J. Ali, J. L. Belof, L. X. Benedict, J. Bernier, D. Braun, R. Cohen, G. W. Collins, F. Coppari, M. P. Desjarlais, D. Fratanduono, S. Hamel, A. Krygier, A. Lazicki, J. Mcnaney, M. Millot, P. C. Myint, M. G. Newman, J. R. Rygg, D. M. Sterbentz, S. T. Stewart, L. Stixrude, D. C. Swift, C. Wehrenberg, and J. H. Eggert, *Science* **375**, 202 (2022).
- [7] J. A. Hawreliak, D. H. Kalantar, J. S. Stolken, B. A. Remington, H. E. Lorenzana, and J. S. Wark, *Phys. Rev. B* **78**, 220101(R) (2008).
- [8] D. H. Kalantar, J. F. Belak, G. W. Collins, J. D. Colvin, H. M. Davies, J. H. Eggert, T. C. Germann, J. Hawreliak, B. L. Holian, K. Kadau, P. S. Lomdahl, H. E. Lorenzana, M. A. Meyers, K. Rosolankova, M. S. Schneider, J. Sheppard, J. S. Stolken, and J. S. Wark, *Phys. Rev. Lett.* **95**, 075502 (2005).
- [9] R. J. Hemley and H.-K. Mao, *Int. Geol. Rev.* **43**, 1 (2001).
- [10] S. J. Turneaure, S. M. Sharma, and Y. M. Gupta, *Phys. Rev. Lett.* **125**, 215702 (2020).
- [11] R. F. Smith, D. E. Fratanduono, D. G. Braun, T. S. Duffy, J. K. Wicks, P. M. Celliers, S. J. Ali, A. Fernandez-Pañella, R. G. Kraus, D. C. Swift, G. W. Collins, and J. H. Eggert, *Nat. Astron.* **2**, 452 (2018).
- [12] S. Tateno, K. Hirose, T. Komabayashi, H. Ozawa, and Y. Ohishi, *Geophys. Res. Lett.* **39**, 2012GL052103 (2012).
- [13] S. Tateno, K. Hirose, Y. Ohishi, and Y. Tsumi, *Science* **330**, 359 (2010).
- [14] A. Dewaele, C. Denoual, S. Anzellini, F. Occelli, M. Mezouar, P. Cordier, S. Merkel, M. Véron, and E. Rausch, *Phys. Rev. B* **91**, 174105 (2015).
- [15] Y. Kuwayama, K. Hirose, N. Sata, and Y. Ohishi, *Earth Planet. Sci. Lett.* **273**, 379 (2008).
- [16] A. K. McMahan and R. C. Albers, *Phys. Rev. Lett.* **49**, 1198 (1982).
- [17] N. Hirao, Y. Akahama, and Y. Ohishi, *Matter Radiat. Extrem.* **7**, 038403 (2022).
- [18] A. Dewaele, M. Torrent, P. Loubeyre, and M. Mezouar, *Phys. Rev. B* **78**, 104102 (2008).
- [19] S. Boccato, R. Torchio, P. D'Angelo, A. Trapananti, I. Kantor, V. Recoules, S. Anzellini, G. Morard, T. Irifune, and S. Pascarelli, *Phys. Rev. B* **100**, 180101(R) (2019).
- [20] O. T. Lord, I. G. Wood, D. P. Dobson, L. Vočadlo, W. Wang, A. R. Thomson, E. T. Wann, G. Morard, M. Mezouar, and M. J. Walter, *Earth Planet. Sci. Lett.* **408**, 226 (2014).
- [21] R. Torchio, Y. O. Kvashnin, S. Pascarelli, O. Mathon, C. Marini, L. Genovese, P. Bruno, G. Garbarino, A. Dewaele, F. Occelli, and P. Loubeyre, *Phys. Rev. Lett.* **107**, 237202 (2011).
- [22] N. Smirnov, *J. Appl. Phys.* **134**, 025901 (2023).
- [23] Z.-Y. Zeng, C.-E. Hu, L.-C. Cai, and F.-Q. Jing, *Phys. B (Amsterdam, Neth.)* **407**, 330 (2012).
- [24] A. Hausoel, M. Karolak, E. Şaşıoğlu, A. Lichtenstein, K. Held, A. Katanin, A. Toschi, and G. Sangiovanni, *Nat. Commun.* **8**, 16062 (2017).
- [25] L. Dubrovinsky, N. Dubrovinskaia, O. Narygina, I. Kantor, A. Kuznetsov, V. B. Prakapenka, L. Vitos, B. Johansson, A. S. Mikhailushkin, S. I. Simak, and I. A. Abrikosov, *Science* **316**, 1880 (2007).
- [26] R. Torchio, S. Boccato, F. Miozzi, A. D. Rosa, N. Ishimatsu, I. Kantor, N. Sévelin-Radiguet, R. Briggs, C. Meneghini, T. Irifune, and G. Morard, *Geophys. Res. Lett.* **47**, e2020GL088169 (2020).
- [27] J.-F. Lin, V. V. Struzhkin, W. Sturhahn, E. Huang, J. Zhao, M. Y. Hu, E. E. Alp, H. Mao, N. Boctor, and R. J. Hemley, *Geophys. Res. Lett.* **30**, 2112 (2003).
- [28] A. B. Belonoshko, T. Lukinov, J. Fu, J. Zhao, S. Davis, and S. I. Simak, *Nat. Geosci.* **10**, 312 (2017).
- [29] M. Ghosh, S. Zhang, L. Hu, and S. Hu, *J. Phys.: Condens. Matter* **35**, 154002 (2023).
- [30] S. Chatterjee, S. Ghosh, and T. Saha-Dasgupta, *Minerals* **11**, 258 (2021).
- [31] R. McQueen and S. Marsh, *J. Geophys. Res.* **71**, 1751 (1966).
- [32] S. Tecklenburg, R. Colina-Ruiz, S. Hok, C. Bolme, E. Galtier, E. Granados, A. Hashim, H. J. Lee, S. Merkel, and B. Morrow, *Minerals* **11**, 567 (2021).
- [33] T. Katsura, A. M. Nakamura, A. Takabe, T. Okamoto, K. Sangen, S. Hasegawa, X. Liu, and T. Mashimo, *Icarus* **241**, 1 (2014).
- [34] S. Marchi, D. Durda, C. Polanskey, E. Asphaug, W. Bottke, L. Elkins-Tanton, L. Garvie, S. Ray, S. Chocron, and D. Williams, *J. Geophys. Res. Planets* **125**, e2019JE005927 (2020).
- [35] M. D. Furnish, G. T. Gray III, and J. L. Remo, *AIP Conf. Proc.* **309**, 819 (1994).
- [36] N. Bezaeva, D. Badyukov, J. Feinberg, M. Kars, and A. Kosterov, *Analytical Chemistry, and Planetary Sciences: 75th Anniversary of the Vernadsky Institute of the Russian Academy of Sciences* (Springer International Publishing, Cham, 2023), pp. 335–350.
- [37] M. E. Bennett III and H. Y. McSween, *Meteorit. Planet. Sci.* **31**, 255 (1996).
- [38] E. Ohtani, T. Sakurabayashi, and K. Kurosawa, *Prog. Earth Planet. Sci.* **9**, 24 (2022).
- [39] C.-E. Guillaume, *J. Phys. Theor. Appl.* **7**, 262 (1898).
- [40] L. Chen, D. C. Swift, R. A. Austin, J. N. Florando, J. Hawreliak, A. Lazicki, M. D. Saculla, D. Eakins, J. V. Bernier, and M. Kumar, *AIP Conf. Proc.* **1793**, 110008 (2017).

- [41] R. A. Graham, D. H. Anderson, and J. R. Holland, *J. Appl. Phys.* **38**, 223 (1967).
- [42] D. R. Curran, *J. Appl. Phys.* **32**, 1811 (1961).
- [43] D. D. Meyerhofer, J. Bromage, C. Dorrer, J. H. Kelly, B. E. Kruschwitz, S. J. Loucks, R. L. McCrory, S. F. B. Morse, J. F. Myatt, P. M. Nilson, J. Qiao, T. C. Sangster, C. Stoeckl, L. J. Waxer, and J. D. Zuegel, *J. Phys.: Conf. Ser.* **244**, 032010 (2010).
- [44] F. Coppari, R. Smith, D. Thorn, J. Rygg, D. Liedahl, R. Kraus, A. Lazicki, M. Millot, and J. Eggert, *Rev. Sci. Instrum.* **90**, 125113 (2019).
- [45] J. R. Rygg, J. H. Eggert, A. E. Lazicki, F. Coppari, J. A. Hawreliak, D. G. Hicks, R. F. Smith, C. M. Sorce, T. M. Uphaus, B. Yaakobi, and G. W. Collins, *Rev. Sci. Instrum.* **83**, 113904 (2012).
- [46] J. Rygg, R. Smith, A. Lazicki, D. Braun, D. Fratanduono, R. Kraus, J. McNaney, D. Swift, C. Wehrenberg, F. Coppari, M. F. Ahmed, M. A. Barrios, K. J. M. Blobaum, G. W. Collins, A. L. Cook, P. Di Nicola, E. G. Dzenitis, S. Gonzales, B. F. Heidl, M. Hohenberger, A. House, N. Izumi, D. H. Kalantar, S. F. Khan, T. R. Kohut, C. Kumar, N. D. Masters, D. N. Polsin, S. P. Regan, C. A. Smith, R. M. Vignes, M. A. Wall, J. Ward, J. S. Wark, T. L. Zobrist, A. Arsenlis, and J. H. Eggert, *Rev. Sci. Instrum.* **91**, 043902 (2020).
- [47] A. Meadowcroft, C. Bentley, and E. Stott, *Rev. Sci. Instrum.* **79**, 113102 (2008).
- [48] P. M. Celliers, D. K. Bradley, G. W. Collins, D. G. Hicks, T. R. Boehly, and W. J. Armstrong, *Rev. Sci. Instrum.* **75**, 4916 (2004).
- [49] L. E. Kirsch, S. J. Ali, D. E. Fratanduono, R. G. Kraus, D. G. Braun, A. Fernandez-Pañella, R. F. Smith, J. M. McNaney, and J. H. Eggert, *J. Appl. Phys.* **125**, 175901 (2019).
- [50] S. Rothman and J. Maw, *J. Phys. IV France* **134**, 745 (2006).
- [51] J.-P. Davis, M. D. Knudson, L. Shulenburg, and S. D. Crockett, *J. Appl. Phys.* **120**, 165901 (2016).
- [52] R. S. McWilliams, J. H. Eggert, D. G. Hicks, D. K. Bradley, P. M. Celliers, D. K. Spaulding, T. R. Boehly, G. W. Collins, and R. Jeanloz, *Phys. Rev. B* **81**, 014111 (2010).
- [53] D. K. Bradley, J. H. Eggert, R. F. Smith, S. T. Prisbrey, D. G. Hicks, D. G. Braun, J. Biener, A. V. Hamza, R. E. Rudd, and G. W. Collins, *Phys. Rev. Lett.* **102**, 075503 (2009).
- [54] See Supplemental Material at <http://link.aps.org/supplemental/10.1103/PhysRevB.109.214112> for comparisons to candidate structures.
- [55] S. Boccato, R. Torchio, I. Kantor, G. Morard, S. Anzellini, R. Giampaoli, R. Briggs, A. Smareglia, T. Irifune, and S. Pascarelli, *J. Geophys. Res. Solid Earth* **122**, 9921 (2017).
- [56] J. Wang, R. F. Smith, J. H. Eggert, D. G. Braun, T. R. Boehly, J. R. Patterson, P. M. Celliers, R. Jeanloz, G. W. Collins, and T. S. Duffy, *J. Appl. Phys.* **114**, 023513 (2013).
- [57] D. N. Polsin, D. E. Fratanduono, J. R. Rygg, A. Lazicki, R. F. Smith, J. H. Eggert, M. C. Gregor, B. H. Henderson, J. A. Delettrez, R. G. Kraus, P. M. Celliers, F. Coppari, D. C. Swift, C. A. McCoy, C. T. Seagle, J. P. Davis, S. J. Burns, G. W. Collins, and T. R. Boehly, *Phys. Rev. Lett.* **119**, 175702 (2017).
- [58] D. Polsin, D. Fratanduono, J. Rygg, A. Lazicki, R. Smith, J. Eggert, M. Gregor, B. Henderson, X. Gong, and J. Delettrez, *Phys. Plasmas* **25**, 082709 (2018).
- [59] S. J. Turneaure, S. M. Sharma, T. J. Volz, J. M. Winey, and Y. M. Gupta, *Sci. Adv.* **3**, eaao3561 (2017).
- [60] M. Sims, R. Briggs, T. J. Volz, S. Singh, S. Hamel, A. L. Coleman, F. Coppari, D. J. Erskine, M. G. Gorman, B. Sadigh, J. Belof, J. H. Eggert, R. F. Smith, and J. K. Wicks, *J. Appl. Phys.* **132**, 075902 (2022).
- [61] O. E. Petel and F. X. Jetté, *Shock Waves* **20**, 73 (2010).
- [62] R. G. Kraus, F. Coppari, D. E. Fratanduono, R. F. Smith, A. Lazicki, C. Wehrenberg, J. H. Eggert, J. R. Rygg, and G. W. Collins, *Phys. Rev. Lett.* **126**, 255701 (2021).
- [63] T. Duffy, N. Madhusudhan, and K. Lee, in *Treatise on Geophysics*, 2nd ed., edited by G. Schubert (Elsevier, Oxford, 2015), Vol. 2, pp. 149–178.
- [64] R. Jago, P. Clark, and P. Rossiter, *Phys. Status Solidi A* **74**, 247 (1982).
- [65] J. Danon, R. Scorzelli, I. Souza-Azevedo, J. Laugier, and A. Chamberod, *Nature (London)* **284**, 537 (1980).
- [66] C. M. Corrigan, K. Nagashima, C. Hilton, T. J. McCoy, R. D. Ash, H. A. Tornabene, R. J. Walker, W. F. McDonough, and D. Rumble, *Geochim. Cosmochim. Acta* **333**, 1 (2022).
- [67] K. L. Rasmussen, D. J. Malvin, V. F. Buchwald, and J. T. Wasson, *Geochim. Cosmochim. Acta* **48**, 805 (1984).
- [68] L. T. Elkins-Tanton and S. Seager, *Astrophys. J.* **688**, 628 (2008).